

# The effect of bath pH on electrodeposition and corrosion properties of ternary Fe-W-Zn alloy platings

Jae-Hyeok Park<sup>1,2</sup>, Takeshi Hagio<sup>1,2</sup>, Yuki Kamimoto<sup>1,2</sup> and Ryoichi Ichino<sup>1,2</sup>

<sup>1</sup>Department of Chemical Systems Engineering, Graduate School of Engineering, Nagoya University, Nagoya, Aichi 464-8601, Japan

<sup>2</sup>Institute of Materials Innovation, Institutes of Innovation for Future Society, Nagoya University, Nagoya, Aichi 464-8601, Japan

Corresponding author e-mail: [hagio@mirai.nagoya-u.ac.jp](mailto:hagio@mirai.nagoya-u.ac.jp)

Tel: +81-52-747-6594 Fax: +81-52-747-6504

## Abstract

As a new trial to improve the corrosion resistance of the Fe-W alloy platings, Fe-W alloys incorporating a small amount of Zn, namely novel ternary Fe-W-Zn alloy platings, are prepared by constant-current electrolysis using citrate-ammonia baths. In this study, the effect of bath pH on elemental composition, morphology, plating structure and corrosion resistance of the electrodeposited ternary alloy platings are investigated. The W content of the electrodeposited alloys showed a maximum of 31.5 at.% at pH 8.0 and an inverse correlation was observed between the W content and current efficiency in the investigated pH range. The Zn content tended to decrease with increasing bath pH, and the structure of alloy platings gradually refined along with the increase in the amount of Zn incorporated into the Fe-W alloy. Potentiodynamic polarization test results reveal fine granular structured ternary Fe-W-Zn alloy prepared at pH 8.0, containing approximately 1.6 at.% of Zn, showed

distinctly enhanced corrosion resistance in a 1M H<sub>2</sub>SO<sub>4</sub> solution compared to binary Fe-W alloy and ternary alloys prepared at pH 6.0, 7.0 and 9.0. It has been found that the bath pH has a great influence on the elemental composition of the ternary alloys, which significantly effects the plating structure and corrosion resistance of the alloy platings.

Keywords: Ternary alloy plating, Fe-W-Zn alloy, Zn content, Plating structure, Corrosion resistance

## 1. Introduction

Recently, interest in electrodeposited W alloy plating has increased. Iron group element-W alloy platings, such as Ni-W, Co-W and Fe-W, are attracting great attention as promising alternatives for chromium (Cr) platings which use toxic hexavalent chromium, owing to their high hardness, wear resistance, corrosion resistance and thermal stability[1–7]. Further, W alloy platings are also gradually expanding its application to various industrial fields such as electrode materials for Li ion batteries[8] and fuel cells[9], micro-electronical systems (MEMS)[10] and magnetic materials[11].

Generally, electrodeposition of metal W from aqueous solution is difficult because tungstate ion predominantly exists as oxyanions such as paratungstates, [HW<sub>6</sub>O<sub>21</sub>]<sup>5-</sup>, metatungstates [H<sub>2</sub>W<sub>21</sub>O<sub>40</sub>]<sup>6-</sup> and tungstate [WO<sub>4</sub><sup>2-</sup>] ion, but the existence of iron-group elements enable W to be co-deposited as alloys based on the principle of induced co-deposition presented by Brenner[12].

Numerous studies have been carried out on the electrodeposition process and properties of alloy platings made from iron-group elements and W, especially on the Ni-W alloys from citrate-ammonia bath [13–17]. Despite the superior properties of the Ni-W alloys, the use of Ni is gradually being avoided due to environmental impact and toxicity to the human body

[18]. Eluted Ni ion from elemental Ni and Ni alloys has been reported as the one of the major cause in triggering skin inflammation or nickel-itch for human skin [19–20]. From this point of view, electrodeposited Fe-W alloys, which use harmless and abundant Fe is gaining considerable interest. Fe-W alloy platings have the advantages of high hardness and high thermal stability compared to Cr and Ni-W platings even at elevated temperatures[21–23]. However, their corrosion resistances are still insufficient to apply for coatings used in harsh industrial environments. Therefore, we propose the incorporation of a third element, Zn, into Fe-W alloys as a solution to improve the corrosion properties of Fe-W alloys based on previous our report [24].

Fundamentally, the electrodeposition mechanisms of Fe-W alloys and the Ni-W alloys are expected to be similar[25]. However, it should be considered that the difference between the electrodeposition of Fe-W and Ni-W alloy system is that Fe has two oxidation states, which may make the bath chemistry more unstable.

Moreover, the electrodeposition mechanisms of ternary alloys are more complicated, especially for those containing elements with distinct deposition potentials. Though various research on binary Fe-W alloy have been reported, details in electrodeposition mechanism of Fe-W alloy, especially on the effects of bath pH, are not well known. Moreover, electrodeposition of ternary Fe-W-Zn platings is a new system proposed by our group. Here, the effects of the bath pH on the elemental compositions, plating structures and corrosion resistances of the electrodeposited ternary Fe-W-Zn alloys are reported for the first time. The electrodeposition mechanism of the ternary alloy is discussed considering knowledge from previous reports on electrodeposition of the binary W alloy. In addition, the corrosion properties of the ternary alloys were evaluated by potentiodynamic polarization test in 1M H<sub>2</sub>SO<sub>4</sub> solution.

## 2. Experimental

### 2.1 Electrodeposition of ternary Fe-W-Zn alloy platings

Ternary Fe-W-Zn alloys were deposited on commercial steel plates (B-60-P01, Yamamoto-MS Co., Ltd) from citrate-ammonia baths. The plating bath for ternary Fe-W-Zn alloys were prepared by mixing  $\text{Na}_3\text{C}_6\text{H}_5\text{O}_7 \cdot 2\text{H}_2\text{O}$ ,  $(\text{NH}_4)_2\text{SO}_4$ ,  $\text{FeSO}_4 \cdot 7\text{H}_2\text{O}$ ,  $\text{Na}_2\text{WO}_4 \cdot 2\text{H}_2\text{O}$  and  $\text{ZnSO}_4 \cdot 7\text{H}_2\text{O}$ . The bath composition of ternary Fe-W-Zn alloys are presented in [Table 1](#). Plating bath of binary Fe-W alloys were also prepared by excluding  $\text{ZnSO}_4 \cdot 7\text{H}_2\text{O}$  from the aforementioned bath recipe for comparison. The total volume of the baths was adjusted to 200 ml by supplementing Ar gas purged distilled water and their temperatures were maintained at 80 °C using a water bath because the overvoltage required for the induced co-deposition of the Fe-W alloy was reduced at higher bath temperatures [24]. The bath pH was adjusted to 6.0, 7.0, 8.0 and 9.0 by using 10 wt.% NaOH solution. Dissolved oxygen was removed from the bath by Ar purging for 30 min prior to electrodeposition.

The steel plates (cathode) were degreased and cleaned with ethanol and 10 wt.%  $\text{H}_2\text{SO}_4$  solution, respectively, before use. The deposition area was adjusted to  $2 \times 2 \text{ cm}^2$  by masking the extra area with an insulation tape. An anode chamber with a cation permeable diaphragm (Nafion® NRE-212, DuPont), filled with dilute  $\text{H}_2\text{SO}_4$  solution, was adopted to prevent oxidation of  $\text{Fe}^{2+}$  and decomposition of organic complexing agents by the anodic reaction. A Pt coil (anode) was set in the anode chamber and Ag/AgCl electrode in saturated KCl solution was used as the reference electrode. A schematic illustration of the electrodeposition system used in this study is shown in [Fig. 1](#).

A potentiogalvanostat (HZ-7000, Hokuto denko) was used for electrodeposition. Linear sweep voltammetry was performed with a scan rate of  $50 \text{ mV} \cdot \text{s}^{-1}$  in each bath pH to verify

the electrodeposition behaviors of ternary alloys. Constant current electrolysis was carried out by applying a fixed current density of  $-20 \text{ mA}\cdot\text{cm}^{-2}$  to prepare the ternary Fe-W-Zn and binary Fe-W alloys. The total amount of applied electric charge,  $Q$ , was set to  $35 \text{ C}\cdot\text{cm}^{-2}$ . The baths were continuously stirred at 500 rpm using a magnetic stirrer during the plating process. Electrodeposition of each plating specimen was repeated at least 3 times per each bath pH condition to confirm the certainty of the data. The cathodic current efficiency ( $C_{\text{eff}}$ ) was calculated based on the mass gain of the cathode and the elemental compositions of the deposited alloy platings using Faraday's Law as follows:

$$C_{\text{eff}} = \frac{\text{mass of the deposits}}{\text{theoretical mass gain}} \times 100 = \frac{w \cdot F}{Q} \sum \frac{C_x \cdot Z_x}{M_x} \times 100 \quad (1)$$

where  $w$  is the mass of the electrodeposited alloys (g),  $F$  is Faraday's constant ( $96,485 \text{ C}\cdot\text{mol}^{-1}$ ),  $Q$  is the passed amount of electric charge (C),  $C_x$  ( $x = \text{Zn, Fe, and W}$ ) is the weight fraction of each element in the alloy,  $Z_x$  is the ionic valence of each element, and  $M_x$  is the atomic weight of each element ( $\text{g}\cdot\text{mol}^{-1}$ ).

## 2.2 Characterization of alloys

Surface morphologies and cross-sectional structure of alloy platings were observed by field-emission scanning electron microscope (FE-SEM, JSM-6330, JEOL). The elemental compositions of alloys were analyzed by energy-dispersive spectroscopy (EDS, SEM-EDX Type N, Hitachi). The composition analysis of the alloy plating using EDS was measured three different parts for the same sample about the metal elements (Fe, W and Zn) excluding or including the oxygen (O) content, separately. Phase analysis of electrodeposited alloys was conducted using X-ray diffractometer (XRD, RINT 2500TTR, Rigaku) equipped with Cu-K $\alpha$  ( $\lambda = 0.15456 \text{ nm}$ ) radiation. The chemical state of metals constituting ternary alloy plating was studied using X-ray photoelectron spectroscopy (XPS, ESCALAB 250Xi,

Thermo scientific) equipped with Al- $k\alpha$  (1486 eV) source. Individual high-resolution scans for W 4f, Fe 2p and Zn LMM were taken at pass energy of 20 eV, in step of 0.05 eV and 50 msec dwell time. Ar etching was carried out in each sample for 300 sec with 4,000 eV Ar ion beam for comparing the oxidation state of metals at plating surface and inner plating layer.

### 2.3 Corrosion tests

Potentiodynamic polarization measurements were carried out in 1M H<sub>2</sub>SO<sub>4</sub> solution at room temperature. The test solution was deaerated with high purity Ar gas for 30 min to remove the dissolved oxygen. The exposed area of the plating specimens was fixed to 1 × 1 cm<sup>2</sup>. Polarization measurements were carried out from -0.3 V (vs. OCP) to +2.5 V (vs. Ag/AgCl) with a scan rate of 1 mV·s<sup>-1</sup>. The open circuit potential (OCP) was stabilized for least 30 min before the polarization measurement, except for the Zn plate. Considering that the corrosion rate of Zn is very high in 1M H<sub>2</sub>SO<sub>4</sub> solution, the polarization test for Zn plate was measured immediately after immersion in the solution. The polarization parameters, such as corrosion potential ( $E_{corr}$ ) and corrosion current density ( $I_{corr}$ ) were calculated from the intersection of the anodic and cathodic Tafel curves employing the Tafel extrapolation methods. And critical current density ( $I_{crit}$ ) and passive current density ( $I_{pass}$ ) were determined from the polarization curves. Polarization measurement was performed at least 2 times for each condition for different samples to confirm reproducibility.

## 3. Results and discussion

### 3.1 Electrodeposition

Figure. 2 shows a series of linear sweep voltammograms measured at bath pH of 6.0 to 9.0. The gradient of the curves decreased and the deposition potential shifted to more cathodic

direction as the bath pH increased. At pH of 8.0 and 9.0, the current started to increase drastically from approximately -1.05 V (vs. Ag/AgCl). This indicates the electrodeposition of the ternary alloys occurs at this potential. This showed the similar results with our previous reports about the electrodeposition of ternary Fe-W-Zn alloy plating, which the deposition potential of binary Fe-W alloy was about -1.0 V at bath of pH 8.0, and the addition of Zn into Fe-W bath slightly shifts the deposition potential to more base potential direction [24]. At the pH of 6.0 and 7.0, the current largely increased from around -1.00 V, but an gradual increase in current was also observed from -0.8 V. Considering the speciation diagram of the citric acid[26], the predominant species at pH range of 7.0 to 9.0 is the triply-charged anion  $C_6H_5O_7^{3-}$  ( $Cit^{3-}$ ) that can form complex ions with other metal ions[27]. However, in the plating bath below pH 7.0, the fraction of  $Cit^{3-}$  drastically decreases, and only about 60 % of citrate ions exists as  $Cit^{3-}$  at pH 6.0. Considering the amounts of  $Na_3C_6H_5O_7 \cdot 2H_2O$ ,  $FeSO_4 \cdot 7H_2O$  and  $Na_2WO_4 \cdot 2H_2O$  used in this experiment, the amount of  $Cit^{3-}$  is insufficient for all metal ions to form metal ion-citrate complex at pH 6.0 and 7.0. Therefore, the reduction of metal Fe from the free Fe ions may also accompany with those from the Fe-citrate complexes.

### 3.2 Characterizations

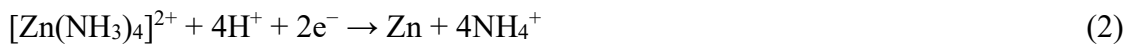
The XPS analysis was conducted for verifying the chemical state of electrodeposited ternary alloy plating. Fig. 3 presents the XPS W 4f core level spectra for ternary alloy plating deposited at bath pH range of 6.0 to 9.0. The standard binding energy for W 4f<sub>7/2</sub> is 36.1 eV ( $WO_3$ ), 33.1 eV ( $WO_2$ ) and 31.6 eV (metal W), respectively. The XPS W 4f spectra of plating specimens before Ar etching shows W exists mainly as  $W^{6+}$  ( $WO_3$ ) at plating surface. This suggest a thick oxide layer including  $WO_3$  is present on the top surface. However, W 4f spectra obtained after Ar etching for 5 min shows W mainly exists as  $W^0$  (metal W) at the

inside of the plating layer, unlike the plating surface. The fraction of  $\text{WO}_3$  at the inside of the plating layer was relatively high in the alloy deposited at pH 6.0, which may originate from the incomplete reduction of tungstate ion ( $\text{WO}_4^{2-}$ ) to metal W owing to insufficient  $\text{Cit}^{3-}$  concentration at this pH. Fig. 4 presents XPS Fe 2p and Zn LMM spectra of ternary alloy plating. The XPS Fe 2p spectra of the plating specimen before Ar etching presented in Fig. 4(a) shows Fe mainly exists as oxidized state ( $\text{Fe}_2\text{O}_3$ , binding energy: 710.8 eV) at the plating surface. However, Fig. 4(b) suggest Fe also exists as a metal Fe ( $\text{Fe}^0$ , binding energy of 706.7 eV) after Ar etching for 5 min. Because Zn shows only a small binding energy shift in the Zn 2p region, Zn LMM Auger peaks were measured instead of Zn 2p spectra [28]. As shown in Fig. 4(c), it was difficult to distinguish the peaks due to various oxidation states, but after Ar etching for 5 min (Fig. 4(d)), the peaks were confirmed around 992 and 995.6 eV as with the peaks of metal Zn confirmed from the reference sample (bulk Zn plate) presented in Fig 4(e). From the XPS analysis results, it was confirmed that the top surface of ternary alloy plating was present in an oxide state, and inner layer was present mostly as a metallic state.

The elemental compositions of metal elements (Fe, W and Zn) of the ternary alloy plating measured by EDS and current efficiencies of ternary alloys are presented in Fig. 5. The reason for measuring only the composition of metal elements excluding the oxygen content of the plating was for analyzing the composition excluding the influence from the oxide layer present on the plating surface confirmed by XPS results. The Zn content of the alloys and current efficiencies were the highest at pH 6.0 while the W content became the lowest value of approximately 17 at.%. Considering the ionization of ammonia shown in Fig. 5(c), almost ammonia in plating bath exists as  $\text{NH}_4^+$  at pH 6.0 and 7.0, which does not form complex ions with Zn. Thus, Zn may exist as a citrate complex ions such as  $[\text{Zn}(\text{Cit})]^-$  (log



$\beta = 5.02$ ) and  $[\text{Zn}(\text{Cit})_2]^{4-}$  ( $\log \beta = 6.76$ )[29], or a ternary complex ions with other co-existing metal ions, such as Cit-Zn-Fe or Cit-Zn- $\text{WO}_4$  complexes. On the other hand, Zn-ammonia complex ions are expected to form above pH 7.0 as the fraction of  $\text{NH}_3$  increases because  $[\text{Zn}(\text{NH}_3)_4]^{2+}$  ( $\log \beta = 9.06$ ) has a higher stability constant than the aforementioned Cit-Zn complex ions [30]. Zn ions are expected to exist as almost  $[\text{Zn}(\text{NH}_3)_4]^{2+}$  at above pH 8.0. In this pH region, metallic Zn can be electrodeposited from the ammonia complex by the following reaction.



However, when the pH is increased to 9.0, Zn content in the alloy plating drastically decreased. This may be attributed to the excess  $\text{NH}_3$  in plating bath. Accounting to Fig. 5(c), the fraction of  $\text{NH}_3$  rapidly increases to about 40 % at pH 9.0 and greatly exceeds the amount necessary to form Zn-ammonia complex ions. The excess  $\text{NH}_3$  may stabilize  $[\text{Zn}(\text{NH}_3)_4]^{2+}$  and suppress the reduction of  $[\text{Zn}(\text{NH}_3)_4]^{2+}$  to metallic Zn. Meanwhile, W content showed no clear correlation between the Zn content, implying an independent deposition process of W and Zn. The W content of the alloy was found to be inversely proportional to the current efficiency. According to previous reports on the iron group element-W alloy platings[26, 31], the deposition precursor of the Fe-W alloy is reported to be the quaternary complex ion  $[(\text{Fe})(\text{WO}_4)(\text{Cit})(\text{H})]^{2-}$ , which is formed when  $[(\text{Fe})(\text{Cit})]^-$  and  $[(\text{WO}_4)(\text{Cit})(\text{H})]^{4-}$  exists according to the following equation.



The W content of the ternary alloy obtained in this study showed close relationship with the fraction of  $[(\text{WO}_4)(\text{Cit})(\text{H})]^{4-}$  at each pH as shown in Fig. 5(d). The relative abundance of

this specie was the highest at pH 8.0, and this corresponded to the W content of the alloy, which was also the highest at this pH value. Decrease in W content at pH 9.0 implies that the metal W precipitates from the mixed-metal complex,  $[(\text{Fe})(\text{WO}_4)(\text{Cit})(\text{H})]^{2-}$  and not  $\text{WO}_4^{2-}$ . The inverse relationship between current efficiency and W content is considered to be due to higher hydrogen evolution reaction (HER) rate at cathode surface during electrodeposition. Because W has a low hydrogen evolution overvoltage, metallic W electrodeposited on the cathode surface can activate the HER. Current efficiency of alloy deposition may have decreased due to consumption of electrons by HER.

Figure 6 shows the X-ray diffractograms for ternary Fe-W-Zn alloy platings and the binary Fe-W alloy plating. All alloys exhibited a single broad peak between  $42.70$  to  $43.88^\circ$ . At the binary Fe-W alloy, this broad peak represents the incorporation of W into BCC structured Fe lattice, especially at Fe (110) plane ( $2\theta = 44.74^\circ$ ). Considering the fact that the solubility limit of W in bcc Fe is about 14 at.%[32], alloys which contain W content above this value become a typical "amorphous-like" nanocrystalline[6] or amorphous structure[22]. This incorporation enlarged inter-planar spacing of d (110) and can transform the crystallographic structure of electrodeposited Fe[33], which can shift the peak position to lower diffraction angle.

In the XRD patterns of the ternary alloys, the peak intensity was gradually decreased as bath pH decreased from 9.0 to 6.0. This can be attributed to the increase in the Zn content in the ternary alloys, which decrease the crystallinity of the Fe-W alloy structure. However, the tendency of peak position and full wide at half maximum (FWHM) were not coincident with Zn content of alloys. In case of ternary alloy deposited at pH 8.0, the peak position was confirmed at the lowest angle ( $2\theta = 42.70^\circ$ ), and FWHM was the largest ( $7.11^\circ$ ). This can

be assumed that the peak position and FWHM of ternary alloys are affected by both W and Zn content of the alloy.

[Figure. 7](#) shows the surface FE-SEM images of alloy platings electrodeposited at various bath pH. All alloy platings obtained in this pH ranges showed a rather smooth surface even though no additives were added into the plating bath. Some small particles were found to be irregularly distributed on the surface of the platings obtained at pH 6.0 and 7.0. Meanwhile, the plating obtained at pH 8.0 exhibited the smoothest surface and the particles observed at pH of 6.0 and 7.0 were hardly recognized. There were also no particles on the surface obtained at pH 9.0; however, the morphology became coarse and the surface irregularity increased.

The FE-SEM images of the fractured cross-sections of the alloy platings are presented in [Fig. 8](#). No clear grains could be obviously observed for the alloy obtained at pH 6.0, which seems reasonable from the weak and broad XRD peak, implying an amorphous-like structure. As the bath pH increased, the cross-sectional structure of plating gradually changed, and fine granular structure was observed at pH 8.0, and a columnar structure was observed at pH 9.0. Considering the relationship between the surface, cross-sectional structure and the elemental composition of the alloys obtained at each pH, it seems that the Zn content has a greater influence on the structural change of the alloys than the W content. Namely, an amorphous-like plating structure is obtained as the Zn content of the alloy approaches approximately 3 at.% (pH 6.0), a fine granular structure when the Zn content is between 1 to 2 at.% (pH 7.0 and 8.0), and a coarse columnar structure similar to that of the binary Fe-W alloy[24] was obtained when the Zn content became less than 1 at.% (pH 9.0), regardless of their W content.

Figure. 9 shows the SEM image and EDS mapping results for the particles irregularly distributed on the surface of the alloy platings prepared from the bath of pH 6.0. These particles were also observed on the platings prepared at pH 7.0. High content of carbon was detected from these particles and metal elements were hardly identified. Considering the starting materials of the plating bath, the only carbon source is the complexing agent;  $\text{Na}_3\text{C}_6\text{H}_5\text{O}_7 \cdot 2\text{H}_2\text{O}$ . The decomposition of citric acid at the anode should not be the cause of the carbon product because the anode chamber was applied in this study. Therefore, it is anticipated that the particles originated from the cathodic reaction of citric acid. The incomplete reduction of metals from the metal-citrate complex ions at cathode surface may have generated these particles having a high carbon content. In contrast, from bath pH of 8.0 or higher, where Zn can form stable complex ions with ammonia, such particles were hardly found. Therefore, it was presumed that the particles were generated by the incomplete reduction of citrate-Zn-X ternary complex ions ( $\text{X} = \text{Fe}$  or  $\text{WO}_4^{2-}$ ), which are not deposition precursors for metal Zn or Fe-W alloy. The increase in abundance ratio of  $\text{NH}_3$  in the plating bath by the pH change shall promote the formation of Zn-ammonia complex ions in place of ternary citrate-Zn-X complex ions and thus prevent the carbon generation from incomplete reduction of the citrate-Zn-X complex ions.

### 3.3 Corrosion tests

Figure. 10 shows the potentiodynamic polarization curves of the ternary alloy platings and reference materials, namely binary Fe-W plating, W plate, Fe plate and Zn plate, in 1M  $\text{H}_2\text{SO}_4$  solution. In Fig. 10(a), the ternary alloys exhibited an  $E_{\text{corr}}$  around -0.294 to -0.331 V and showed similar value as that of the binary Fe-W alloy (W content: 33.5 at.%) of -0.335 V. Increase in Zn content of the alloys may decrease the  $E_{\text{corr}}$  due to the lower redox potential of Zn (-0.76 V /vs. SHE) than those of Fe (-0.44 V /vs. SHE) and W (+0.1 V /vs.

SHE); however, the trend of  $E_{\text{corr}}$  and the Zn content of the ternary alloy did not match. The W content seemed to be mainly responsible for the  $E_{\text{corr}}$  of the alloys. Generally, W has a more noble potential than Fe, but W-base alloys showed more base (lower) potential as the W content of the alloy increases, caused by  $\text{WO}_3$  formation on the surface in an acidic environment[34]. Therefore, the  $E_{\text{corr}}$  of the ternary alloy obtained at pH 8.0 containing the highest W content (31.5 at.%) must have shown the lowest  $E_{\text{corr}}$  of -0.331 V among the ternary alloys.

While the  $E_{\text{corr}}$  was mainly determined by the W content of the alloys, the  $I_{\text{corr}}$  of the alloys seemed to be greatly affected by the Zn content. The ternary alloy obtained at pH 9.0, which had the lowest Zn content and relatively high W content of 0.59 at.% and 30.15 at.%, respectively, exhibited a lower  $I_{\text{corr}}$  ( $2.46 \times 10^3 \mu\text{A}\cdot\text{cm}^{-2}$ ) than the binary Fe-W alloy ( $6.69 \times 10^3 \mu\text{A}\cdot\text{cm}^{-2}$ ) with a higher W content of 33.5 at.%. Moreover, the ternary alloys obtained at pH 7.0 and 8.0 having a moderate Zn content of around 1.7 at.% showed further lower  $I_{\text{corr}}$  ( $9.27 \times 10^1$  and  $2.96 \times 10^1 \mu\text{A}\cdot\text{cm}^{-2}$ ) and significantly improved passivation properties. This implies that the W content does not determine the  $I_{\text{corr}}$  value and that a small incorporation of Zn can significantly improve the corrosion property of the Fe-W alloy. On the other hand, the alloy obtained at pH 6.0, having the lowest W content (17.6 at.%) and highest Zn content (3.1 at.%), showed the largest  $I_{\text{corr}}$  ( $3.48 \times 10^3 \mu\text{A}\cdot\text{cm}^{-2}$ ) among the alloys. This result well-demonstrates that the corrosion resistance of the alloy is improved until the Zn content reaches around 1.5 to 2 at.% and deteriorates when further Zn is incorporated as shown in Fig. 11. The structural change of the platings by the Zn incorporation may be the possible reason for the change in corrosion properties of the alloys. The plating structures of the ternary alloys gradually change from columnar structure to fine granular structure by the incorporation of Zn to the binary Fe-W alloy structure as presented in Fig. 8. The corrosion

resistance and passivation properties of the ternary alloys exhibited the best performance when its structure became fine granular structure. According to Ashassi-Sorkhabi et al.[35], since a long and straight plating structure can be an appropriate path for corrosion progress, corrosion resistance can be improved if such a corrosion path is shortened by changing in the microstructure of plating.

The ternary alloys obtained at pH 7.0, 8.0 and 9.0 not only showed low  $I_{\text{corr}}$  values but also low  $I_{\text{crit}}$  values. These alloys showed a unique passivation behavior in the potential range of -0.16 to +0.58 V, which was not observed for the binary Fe-W alloy. It can be assumed that this passivation region was formed by incorporating Zn into a binary Fe-W alloy. However, polarization curve of Zn plate in Fig. 10(b) did not exhibit the passive region in this potential range. The corrosion rate of Zn plate in 1M H<sub>2</sub>SO<sub>4</sub> solution was very fast. Despite this fact, the ternary Fe-W-Zn alloy with a small amount of Zn incorporation exhibited remarkably improved corrosion resistance compare to the binary Fe-W alloy. Thus, structural change of alloy platings by Zn addition to binary alloys seemed to be the important factor for improving passivation properties. After this first passivation, a second passivation region continuously appeared, showing similar behaviors to binary Fe-W alloy, but alloys prepared at pH 7.0 and 8.0 showed lower  $I_{\text{pass}}$  than binary alloy. Especially, the passivation proceeded immediately for the alloy obtained at pH 8.0, indicating its excellent corrosion property among all conditions.

After the passivation regions, Fe plate, binary Fe-W and ternary Fe-W-Zn alloys showed rapidly increased current from near the +1.7 V. However, this was not appeared on W plate until +2.5 V, indicating the trans-passivation potential of Fe correspond to +1.7 V. Therefore, selective dissolution of Fe from Fe-W and Fe-W-Zn alloys start from this potential. In the region above this potential, the increase in current tends to be kept lower than that of the

binary alloy in the case of the ternary alloy obtained at pH 7.0 to 9.0. This means that ternary alloys have a lower Fe elution rate than binary alloys after the trans-passivation of Fe. In conclusion, the effect of improvement of the corrosion resistance was appeared when incorporation amount of Zn into Fe-W alloy increased until 2 at.% and showed the critical point when the Zn content is between 1.5 to 2 at.%. The parameters for polarization measurements are summarized in [Table 2](#) and [Fig. 11](#).

Elemental composition of binary Fe-W and ternary Fe-W-Zn alloy before and after polarization test was analyzed by EDS, and the results are shown in the [Table 3](#). After polarization measurement up to +2.5 V, Fe and Zn are expected to be gradually eluted from the corroding surface because +2.5 V is much higher potential region than that of trans-passive region of these metals. However, W may exist as  $WO_3$  state at plating surface due to the wide passivation region of metal W, which can be supported by the polarization test results in [Fig.10 \(b\)](#). Therefore, it is anticipated that the high oxygen content after the polarization measurement is due to the formed  $WO_3$  film on the plating surface, and this can act as a protective layer from corrosive media. The optical photographs of both Fe-W and Fe-W-Zn alloy platings after polarization test are shown in [Fig. 12](#).

The surface FE-SEM images of ternary binary Fe-W alloy and Fe-W-Zn after polarization test until +2.5 V were presented in [Fig. 13](#). In the low magnification SEM image of the Fe-W alloy in [Fig. 13 \(a\)](#), there were several areas where cracks were seen on the surface. In area 1 shown in [Fig. 13 \(b\)](#), a number of fine cracks existed along with enlarged pin hole. Even in area 2, as shown in [Fig. 13 \(c\)](#), the destruction of the coating layer was extensively progressing. On the other hand, in the low magnification SEM image of the ternary alloy electrodeposited at pH 8.0 shown in [Fig. 13 \(d\)](#), the surface was relatively clean even after the polarization measurement. In area 3 of [Fig. 13 \(e\)](#), a small pin hole existed, but its size

was much smaller, and the surrounding cracks did not spread widely compared to binary Fe-W plating. In addition, area 4 shown in Fig. 13 (f) exhibited a clean surface that was hardly damaged by corrosion. The ternary alloy proved to be superior corrosion resistance compared to the binary alloy in severe 1M H<sub>2</sub>SO<sub>4</sub> solution.

#### **4. Conclusions**

In this study, the effect of bath pH on elemental composition, morphology, structure and corrosion resistance of electrodeposited Fe-W-Zn alloy platings were investigated. A clear relationship was found between the bath pH and the elemental composition of the ternary alloy. The Zn content of the alloys was anticipated to be dependent on the type of Zn complex, where a change from the Cit-Zn complex to the Zn-NH<sub>3</sub> complex was expected above pH 8.0. The alloy obtained at pH 8.0 with 1.6 at.% Zn exhibited a smooth surface morphology and fine granular structure, but further increase in pH to 9.0 induced excess amount of free NH<sub>3</sub>, making deposition of Zn more difficult, thereby reducing the Zn content in alloys. The W content of the ternary alloy showed direct relation to the fraction of [(WO<sub>4</sub>)(Cit)(H)]<sup>4-</sup> complex, which is the deposition precursor of W, not a tungstate ion (WO<sub>4</sub><sup>2-</sup>). The plating structure of the alloy gradually changed as the Zn content of the alloy increased, and Zn content was found to mainly contributed to crystal refinement than W content. Ternary alloys containing about 1.5 to 2 at.% Zn showed improved passivation properties and enhanced corrosion resistance, while ternary alloy with about 3 at.% Zn and binary Fe-W alloy showed inferior corrosion resistance. It was found that a critical value for Zn content existed to improve the corrosion property of Fe-W-Zn alloy platings.

#### **Acknowledgments**



This work was partially supported by the JST-OPERA Program, Japan [grant number JPMJOP1843] and research grant from Kyosho Hatta foundation, Japan.

## References

1. de Lima-Neto P, Correia AN, Santana RA, Colares RP, Barros EB, Casciano PN, Vaz GL (2010) Morphological, structural, microhardness and electrochemical characterisations of electrodeposited Cr and Ni–W coatings. *Electrochim Acta* 55:2078–2086
2. Wasekar NP, Hebalkar N, Jyothirmayi A, Lavakumar B, Ramakrishna M, Sundararajan G (2020) Influence of pulse parameters on the mechanical properties and electrochemical corrosion behavior of electrodeposited Ni-W alloy coatings with high tungsten content. *Corros Sci* 165:108409
3. Capel H, Shipway PH, Harris SJ (2003) Sliding wear behaviour of electrodeposited cobalt–tungsten and cobalt–tungsten–iron alloys. *Wear* 255:917–923
4. Weston DP, Shipway PH, Harris SJ, Cheng MK (2009) Friction and sliding wear behaviour of electrodeposited cobalt and cobalt–tungsten alloy coatings for replacement of electrodeposited chromium. *Wear* 267:934–943
5. Nicolenco A, Tsyntaru N, Cesiulis H (2017) Fe (III)-based ammonia-free bath for electrodeposition of Fe-W alloys. *J Electrochem Soc* 164:590–596
6. Oliveira, ALM, Costa JD, de Sousa MB, Alves JJN, Campos ARN, Santana RAC, Prasad S (2015) Studies on electrodeposition and characterization of the Ni–W–Fe alloys coatings. *J Alloys Compd* 619:697–703
7. He F, Yang J, Lei T, Gu C (2007) Structure and properties of electrodeposited Fe–Ni–W alloys with different levels of tungsten content: A comparative study. *Appl Surf Sci* 253:7591–7598
8. Su C, Ye M, Zhon L, Hou J, Li J, Guo J (2016) Oxidation of Fe–W alloy electrodeposits for application to anodes as lithium ion batteries. *Surf Rev Lett* 23:1550100
9. Tharamani CN, Beera P, Jayaram V, Begum NS, Mayanna SM (2006) Studies on electrodeposition of Fe–W alloys for fuel cell applications. *Appl Surf Sci* 253:2031–2037
10. Shacham-Diamand Y, Sverdlov Y (2000) Electrochemically deposited thin film alloys for ULSI and MEMS applications. *Microelectron Eng* 50:525–531
11. Tamilarasan K (2015) Effect of current density on electrodeposited ferrous tungsten thin films. *Indian J Pure Appl Phys* 52:395–398
12. Brenner A (1963) *Electrodeposition of Alloys: Practical and specific information*. Academic Press, New York

13. Allahyarzadeh MH, Aliofkhazraei M, Rouhaghdam AS, Torabinejad V, Alimadadi H, Ashrafi A (2017) Electrodeposition mechanism and corrosion behavior of multilayer nanocrystalline nickel-tungsten alloy. *Electrochim Acta* 258:883–899
14. Kumar KA, Kalaignan GP, Muralidharan VS (2012) Pulse electrodeposition and characterization of nano Ni–W alloy deposits. *Appl Surf Sci* 259:231–237
15. Sassi W, Dhouibi L, Berçot P, Rezrazi M, Triki E (2012) Comparative study of protective nickel–tungsten deposit behavior obtained by continuous and pulsed currents from citrate–ammonia media. *Surf Coatings Technol* 206:4235–4241
16. Vamsi MVN, Wasekar NP, Sundararajan G (2017) Influence of heat treatment on microstructure and mechanical properties of pulse electrodeposited Ni-W alloy coatings. *Surf Coatings Technol* 319:403–414
17. Wang S, Zeng C, Ling Y, Wang J, Xu G (2016) Phase transformations and electrochemical characterizations of electrodeposited amorphous Fe–W coatings. *Surf Coatings Technol* 286:36–41
18. Raval NP, Shah PU, Shah NK (2016) Adsorptive removal of nickel (II) ions from aqueous environment: a review. *J Environ Manage* 179:1–20
19. Goldenberg A, Admani S, Pelletier JL, Jacob SE (2015) Belt buckles—Increasing awareness of nickel exposure in children: A case report. *Pediatrics* 136:691–693
20. Thyssen JP (2011) Nickel and cobalt allergy before and after nickel regulation—evaluation of a public health intervention. *Contact Dermatitis* 65:1–68
21. Mulone A, Nicolenco A, Fornell J, Pellicer E, Tsyntaru N, Cesiulis H, Sort J, Klement U (2018) Enhanced mechanical properties and microstructural modifications in electrodeposited Fe-W alloys through controlled heat treatments. *Surf Coatings Technol* 350:20–30
22. Mulone A, Nicolenco A, Hoffmann V, Klement U, Tsyntaru N, Cesiulis H (2018) In-depth characterization of as-deposited and annealed Fe-W coatings electrodeposited from glycolate-citrate plating bath. *Electrochim Acta* 261:167–177
23. de Lima-Neto P, da Silva GP, Correia AN (2006) A comparative study of the physicochemical and electrochemical properties of Cr and Ni–W–P amorphous electrocoatings. *Electrochim Acta* 51:4928–4933
24. Park J.H, Hagio T, Kamimoto Y, Ichino R (2020) Electrodeposition of a Novel Ternary Fe-W-Zn Alloy: Tuning Corrosion Properties of Fe-W Based Alloys by Zn Addition. *J Electrochem Soc* 167:132508
25. Eliaz N, Gileadi E (2008) Induced codeposition of alloys of tungsten, molybdenum and rhenium with transition metals. In: *Modern aspects of electrochemistry*. Springer, New York
26. Younes O, Gileadi E (2002) Electroplating of Ni/W alloys I. Ammoniacal citrate baths. *J Electrochem Soc* 149:100–111
27. Sillen LG, Martell AE, Bjerrum J (1964) Stability constants of metal-ion complexes. Chemical Society, London

28. Winiarski J, Tylus W, Lutz A, De-Graeve I, Szczygiel B (2018) The study on the corrosion mechanism of protective ternary ZnFeMo alloy coatings deposited on carbon steel in 0.5 mol dm<sup>-3</sup> NaCl solution. *Corros. Sci* 138:130-141
29. Capone S, De Robertis A, De Stefano C, Sammartano S (1986) Formation and stability of zinc (II) and cadmium (II) citrate complexes in aqueous solution at various temperatures. *Talanta* 33:763–767
30. Rodriguez-Torres I, Valentin G, Lopicque F (1999) Electrodeposition of zinc–nickel alloys from ammonia-containing baths. *J Appl Electrochem* 29:1035–1044
31. Gileadi E, Eliaz N (2007) The mechanism of induced codeposition of Ni-W alloys. *ECS Trans* 2:337–349
32. Lassner E, Schubert WD (1999) Tungsten-Properties, chemistry, technology of the element, alloys, and chemical compounds. Vienna University of Technology, Vienna
33. Tsyntsar N, Bobanova J, Ye X, Cesiulis H, Dikusar A, Prosycevas I, Celis JP (2009) Iron–tungsten alloys electrodeposited under direct current from citrate–ammonia plating baths. *Surf Coatings Technol* 203:3136–3141
34. Aljohani TA, Hayden BE (2013) A simultaneous screening of the corrosion resistance of Ni–W thin film alloys. *Electrochim Acta* 111:930–936
35. Ashassi-Sorkhabi H, Es’haghi M (2013) Corrosion resistance enhancement of electroless Ni-P coating by incorporation of ultrasonically dispersed diamond nanoparticles. *Corrosion science* 77:185–193

**Table list**

**Table 1** Bath compositions for ternary Fe-W-Zn alloy plating.

**Table 2** Polarization measurements parameters for the ternary Fe-W-Zn and binary Fe-W alloys in deaerated 1M H<sub>2</sub>SO<sub>4</sub> solution.

**Table 3** Elemental composition of the binary and ternary alloys before and after polarization test.

**Table 1** Bath compositions for ternary Fe-W-Zn alloy plating.

Reagent	Concentration (mol·dm <sup>-3</sup> )
Na <sub>3</sub> C <sub>6</sub> H <sub>5</sub> O <sub>7</sub>	0.26
(NH <sub>4</sub> ) <sub>2</sub> SO <sub>4</sub>	0.8
FeSO <sub>4</sub>	0.2
Na <sub>2</sub> WO <sub>4</sub>	0.05
ZnSO <sub>4</sub>	0.01

**Table 2** Polarization measurements parameters for the ternary Fe-W-Zn and binary Fe-W alloys in deaerated 1M H<sub>2</sub>SO<sub>4</sub> solution.

Specimen	$E_{\text{corr}}$ [V]	$I_{\text{corr}}$ [ $\mu\text{A}\cdot\text{cm}^{-2}$ ]	$I_{\text{crit}}$ [ $\mu\text{A}\cdot\text{cm}^{-2}$ ]	$I_{\text{pass}}$ [ $\mu\text{A}\cdot\text{cm}^{-2}$ ]	
				$I^{\text{st}}$	$I^{\text{nd}}$
Fe-W-Zn (pH 6.0)	-0.294	$3.48\times 10^3$	$1.86\times 10^4$	$7.24\times 10^2$	-
Fe-W-Zn (pH 7.0)	-0.295	$9.27\times 10^1$	$3.58\times 10^2$	$9.77\times 10^1$	$2.47\times 10^2$
Fe-W-Zn (pH 8.0)	-0.331	$2.96\times 10^1$	$1.12\times 10^2$	$1.07\times 10^2$	$2.34\times 10^2$
Fe-W-Zn (pH 9.0)	-0.308	$2.46\times 10^2$	$4.48\times 10^2$	$3.20\times 10^2$	$6.62\times 10^2$
Fe-W	-0.335	$6.69\times 10^2$	$7.46\times 10^2$	$9.22\times 10^2$	-

**Table 3** Elemental composition of the binary and ternary alloys before and after polarization test.

composition [at.%]	Binary Fe-W alloy		Ternary Fe-W-Zn alloy	
	before	after	before	after
O	19.8	51.4	23.5	47.4
Fe	52.1	28.1	49.7	32.6
W	28.1	20.5	24.9	18.9
Zn	-	-	1.9	1.1

## Figure captions

Fig. 1 Schematic diagram of plating system equipped with anode chamber used in this study

Fig. 2 Linear sweep voltammograms for ternary Fe-W-Zn alloy plating bath with various pH range.

Fig. 3 XPS W 4f spectra for ternary Fe-W-Zn alloy plating deposited at various bath pH: (a) pH 6.0, (b) pH 7.0, (c) pH 8.0 and (d) pH 9.0.

Fig. 4 XPS Fe 2p and Zn LMM spectra for ternary Fe-W-Zn alloy plating deposited at pH range of 6.0 to 9.0: (a) Fe 2p spectra before Ar etching, (b) Fe 2p spectra after Ar etching for 5 min, (c) Zn LMM spectra before Ar etching, (d) Zn LMM spectra after Ar etching for 5 min and (e) Zn LMM spectra of reference sample (bulk Zn plate).

Fig. 5 The pH dependence of ternary Fe-W-Zn alloy plating: (a) Zn content of alloys, (b) relation between current efficiency and W content of alloys, (c) ionization of ammonium ion ( $pK_a = 9.27$ ), (d) relative abundance for citrate-tungstate complexes at  $[WO_4^{2-}]/[Cit^{3-}] = 1$ , according to Younes O. et al [26].  $[1, 1, x]^{x-5}$  indicating the citrate-tungstate complexes;  $[(WO_4)(Cit)(H)_x]^{x-5}$ , and x indicating the number of protons.

Fig. 6 XRD diffractograms, peak position, peak height and full width at half maximum (FWHM) for ternary Fe-W-Zn alloy plating deposited at various bath pH and binary Fe-W alloy plating deposited at pH 8.0. The intensity (y-axis) of each pattern was same as 400 cps.

Fig. 7 Surface FE-SEM images and magnified images (inside) of ternary alloys obtained at various bath pH: (a) pH 6.0, (b) pH 7.0, (c) pH 8.0 and (d) pH 9.0. Equal amount of electric charge  $Q = 35 \text{ C}\cdot\text{cm}^{-2}$  was applied for all deposits.

Fig. 8 Cross-sectional FE-SEM images of ternary Fe-W-Zn alloys obtained at (a) pH 6.0, (b) pH 7.0, (c) pH 8.0 and (d) pH 9.0. Equal amount of electric charge  $Q= 35 \text{ C}\cdot\text{cm}^{-2}$  was applied for all deposits.

Fig. 9 High magnification FE-SEM image and EDS elemental mapping of carbon (inside image) for Fe-W-Zn alloy surface deposited at bath pH 6.0.

Fig. 10 Potentiodynamic polarization curves measured in deaerated 1M  $\text{H}_2\text{SO}_4$  solution: (a) ternary Fe-W-Zn alloys with binary Fe-W alloy and (b) with comparative materials.

Fig. 11 Corrosion current density ( $I_{\text{corr}}$ ) and typical crystal structures of alloys according to the Zn content.

Fig. 12 Photographs before and after polarization test until +2.5 V: (a) binary Fe-W alloy plating and (b) Ternary Fe-W-Zn alloy plating deposited at pH 8.0. Exposed area for polarization test:  $1 \times 1 \text{ cm}^2$ .

Fig. 13 Surface FE-SEM images after potentiodynamic polarization until +2.5 V: (a) low magnification image of binary Fe-W alloy, (b) enlarged image of area 1, (c) enlarged image of area 2, (d) low magnification image of ternary Fe-W-Zn alloy deposited at pH 8.0, (e) enlarged image of area 3 and (f) enlarged image of area 4.



## Figures

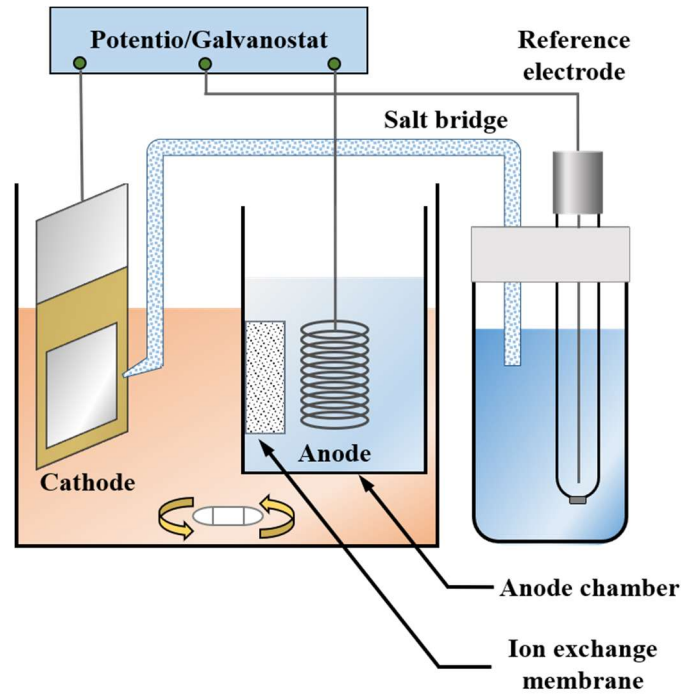


Fig. 1 Schematic diagram of plating system equipped with anode chamber used in this study.

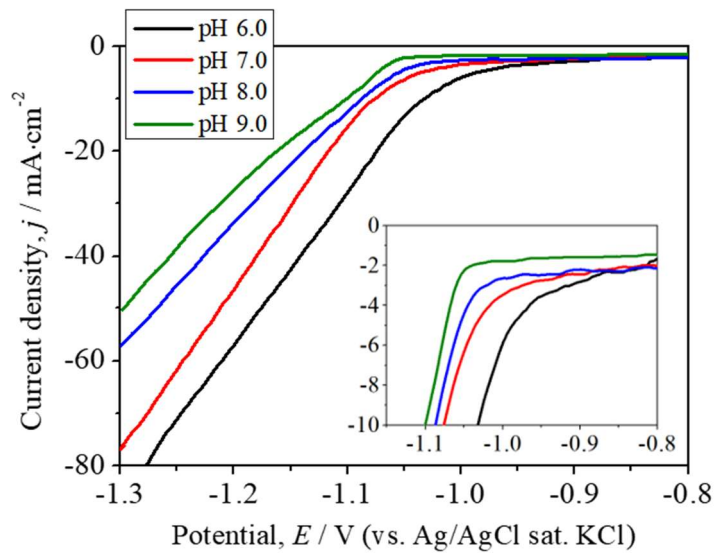


Fig. 2 Linear sweep voltammograms for ternary Fe-W-Zn alloy plating bath with various pH range.

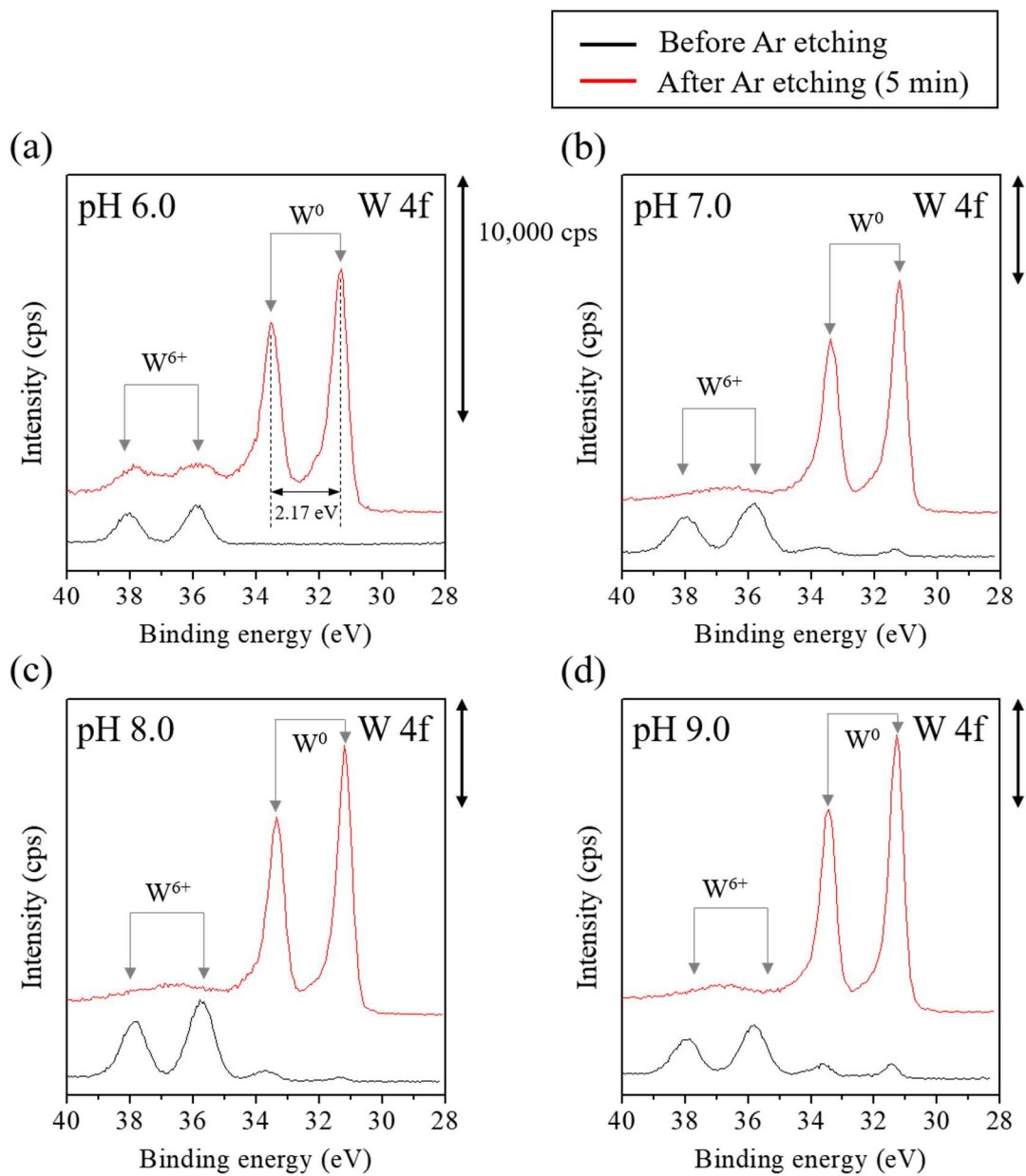


Fig. 3 XPS W 4f spectra for ternary Fe-W-Zn alloy plating deposited at various bath pH: (a) pH 6.0, (b) pH 7.0, (c) pH 8.0 and (d) pH 9.0.

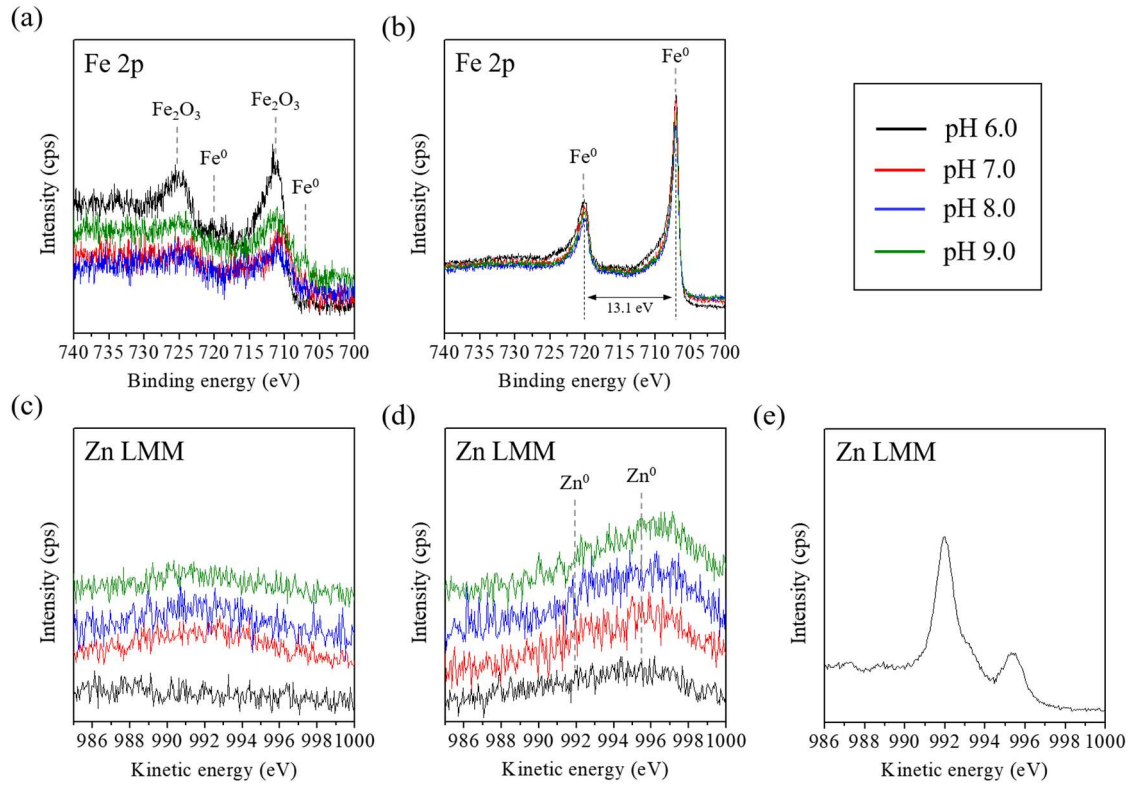


Fig. 4 XPS Fe 2p and Zn LMM spectra for ternary Fe-W-Zn alloy plating deposited at pH range of 6.0 to 9.0: (a) Fe 2p spectra before Ar etching, (b) Fe 2p spectra after Ar etching for 5 min, (c) Zn LMM spectra before Ar etching, (d) Zn LMM spectra after Ar etching for 5 min and (e) Zn LMM spectra of reference sample (bulk Zn plate).

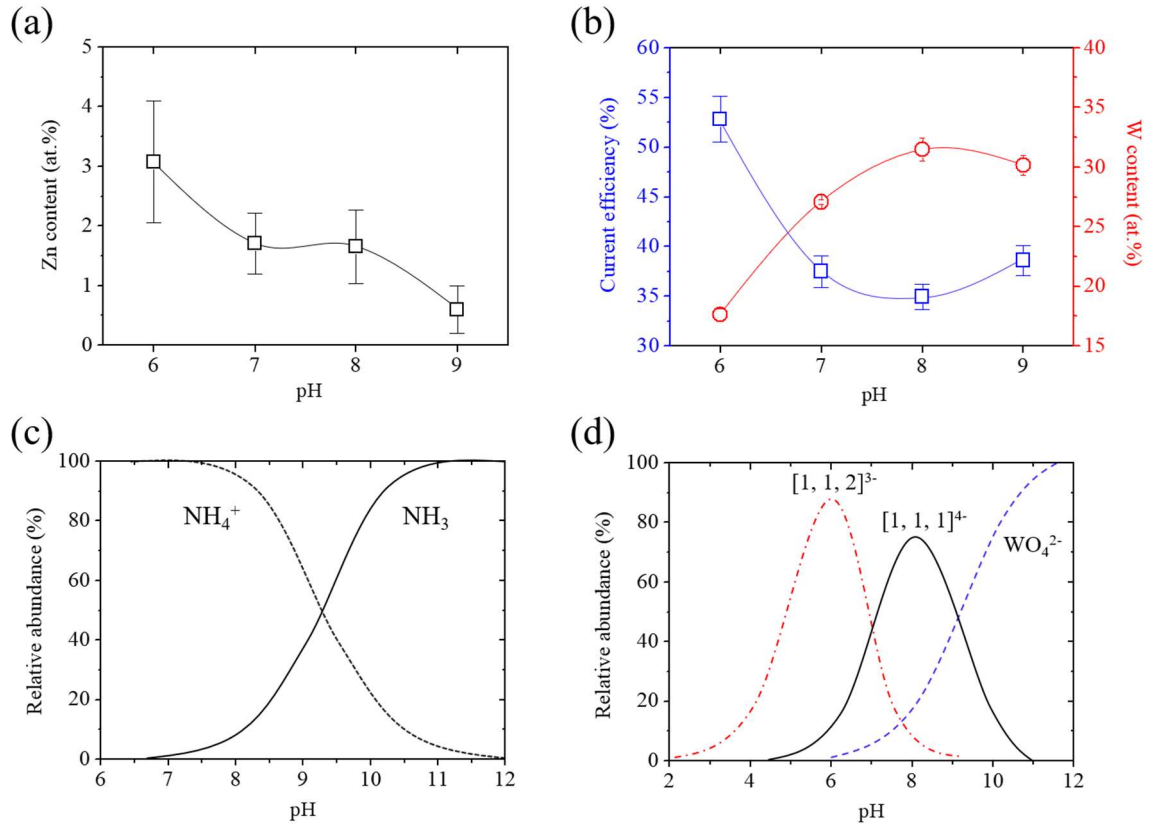


Fig. 5 The pH dependence of ternary Fe-W-Zn alloy plating: (a) Zn content of alloys, (b) relation between current efficiency and W content of alloys, (c) ionization of ammonium ion ( $\text{pK}_a = 9.27$ ), (d) relative abundance for citrate-tungstate complexes at  $[\text{WO}_4^{2-}]/[\text{Cit}^{3-}] = 1$ , according to Younes O. et al [26].  $[1, 1, x]^{x-5}$  indicating the citrate-tungstate complexes;  $[(\text{WO}_4)(\text{Cit})(\text{H})_x]^{x-5}$ , and x indicating the number of protons.

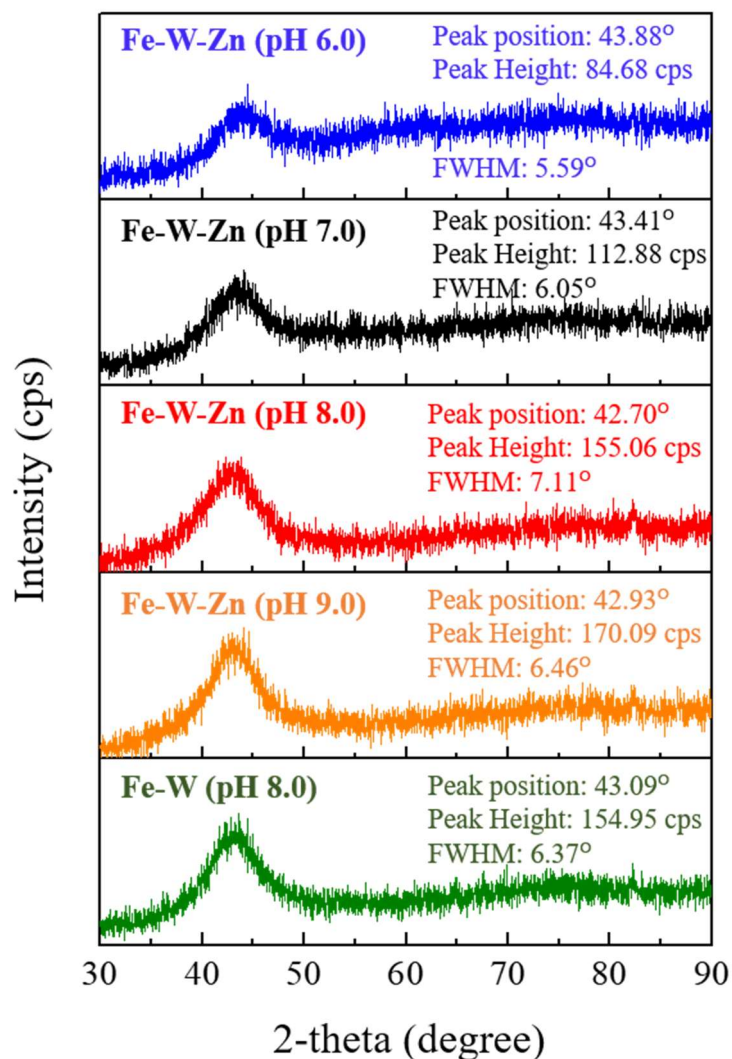


Fig. 6 XRD diffractograms, peak position, peak height and full width at half maximum (FWHM) for ternary Fe-W-Zn alloy plating deposited at various bath pH and binary Fe-W alloy plating deposited at pH 8.0. The intensity (y-axis) of each pattern was same as 400 cps.

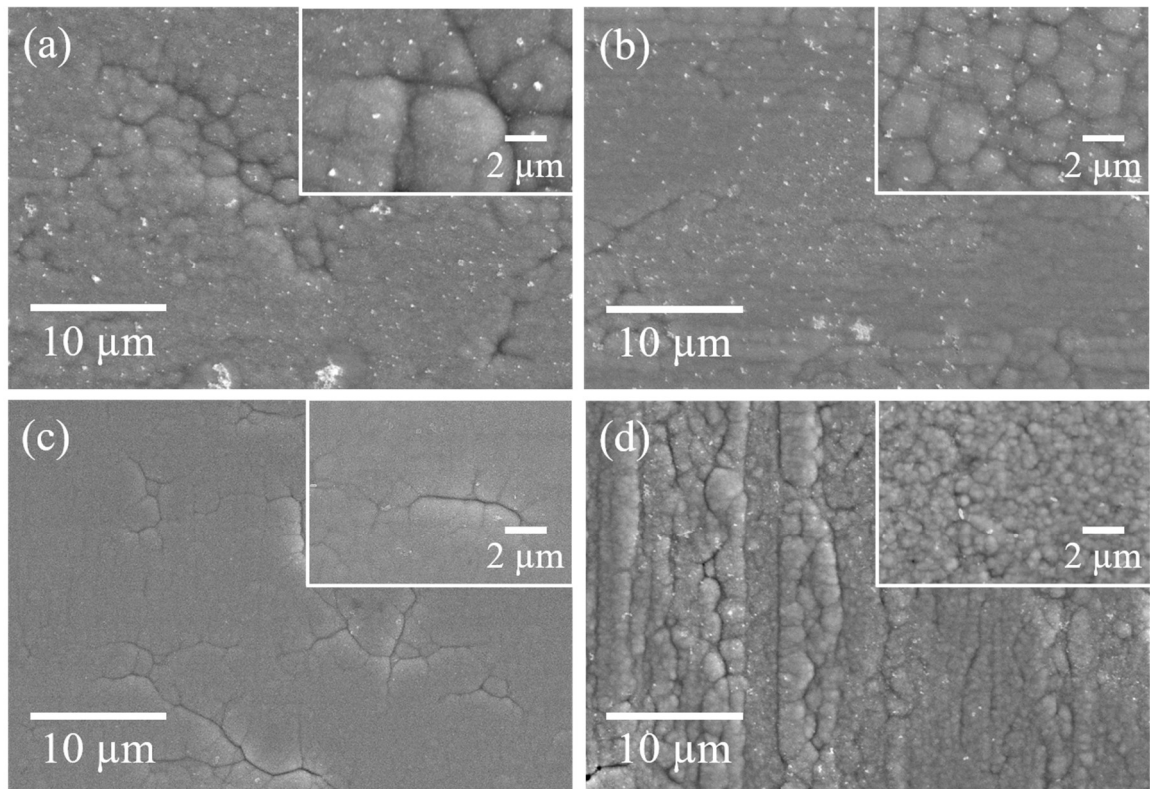


Fig. 7 Surface FE-SEM images and magnified images (inside) of ternary alloys obtained at various bath pH: (a) pH 6.0, (b) pH 7.0, (c) pH 8.0 and (d) pH 9.0. Equal amount of electric charge  $Q=35\text{ C}\cdot\text{cm}^{-2}$  was applied for all deposits.

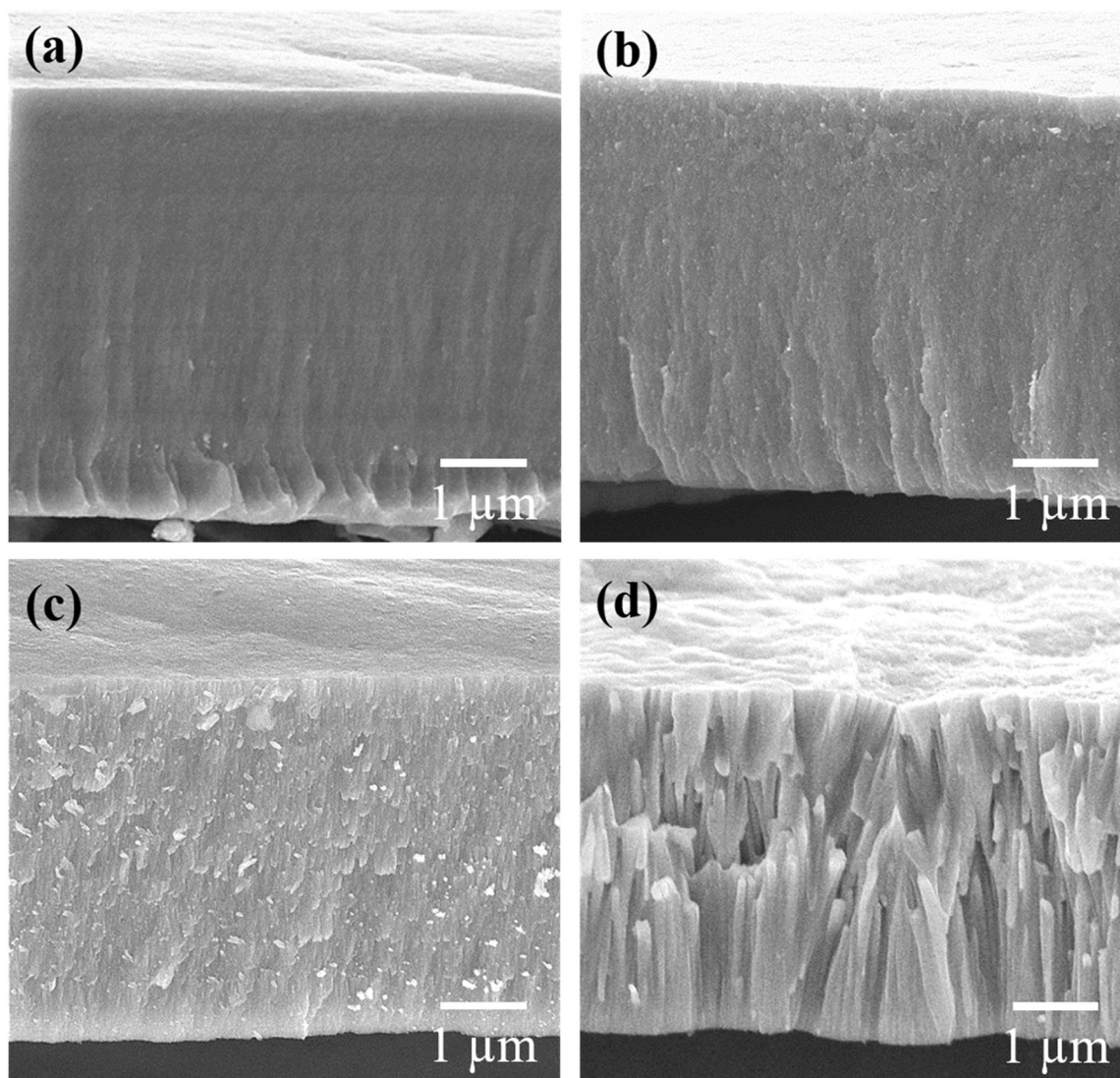


Fig. 8 Cross-sectional FE-SEM images of ternary Fe-W-Zn alloys obtained at (a) pH 6.0, (b) pH 7.0, (c) pH 8.0 and (d) pH 9.0. Equal amount of electric charge  $Q=35\text{ C}\cdot\text{cm}^{-2}$  was applied for all deposits.

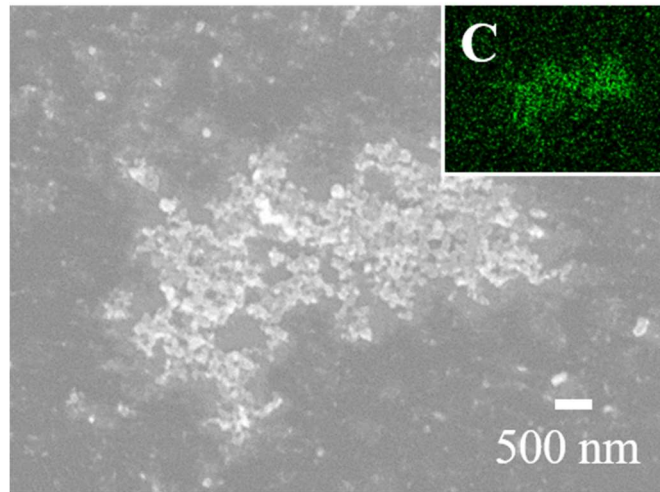


Fig. 9 High magnification FE-SEM image and EDS elemental mapping of carbon (inside image) for Fe-W-Zn alloy surface deposited at bath pH 6.0.



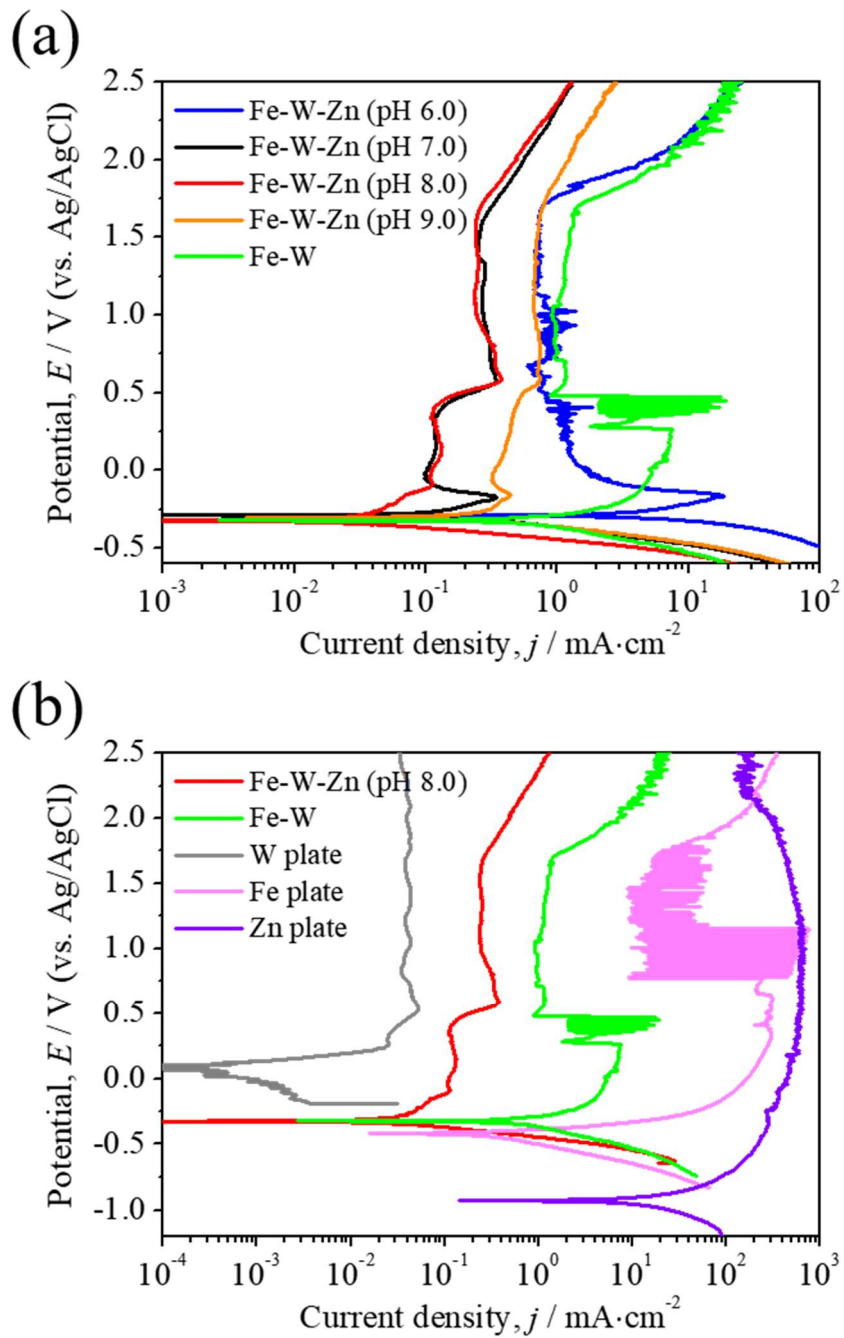


Fig. 10 Potentiodynamic polarization curves measured in deaerated 1M  $\text{H}_2\text{SO}_4$  solution: (a) ternary Fe-W-Zn alloys with binary Fe-W alloy and (b) with comparative materials.

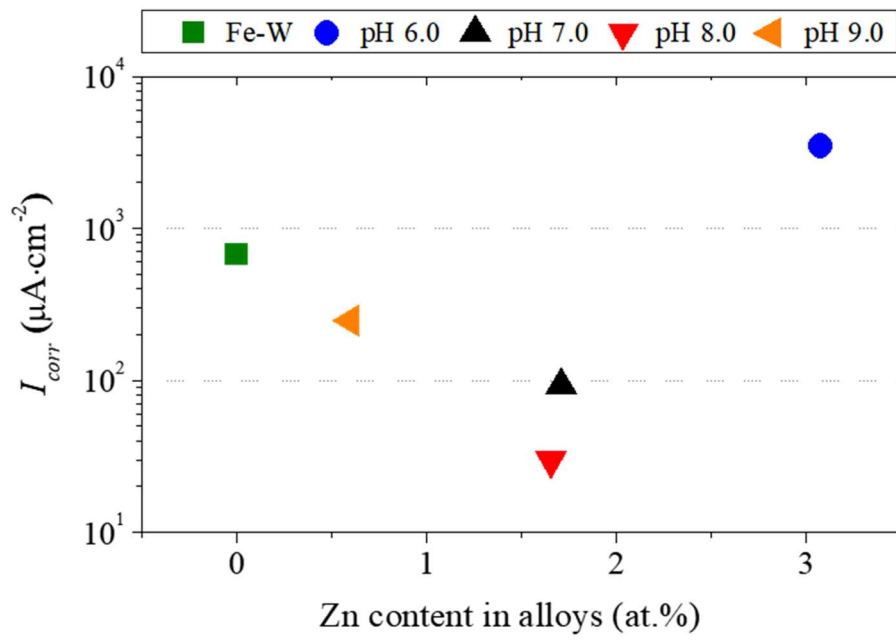


Fig. 11 Corrosion current density ( $I_{corr}$ ) of binary Fe-W and ternary Fe-W-Zn alloys in 1M  $\text{H}_2\text{SO}_4$  solution according to the Zn content.

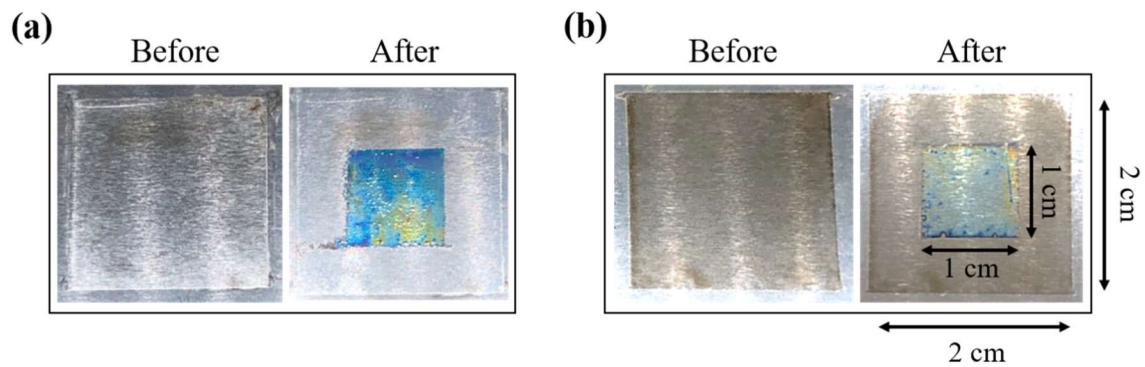


Fig. 12 Photographs before and after polarization test until +2.5 V: (a) binary Fe-W alloy plating and (b) Ternary Fe-W-Zn alloy plating deposited at pH 8.0. Exposed area for polarization test:  $1 \times 1 \text{ cm}^2$ .

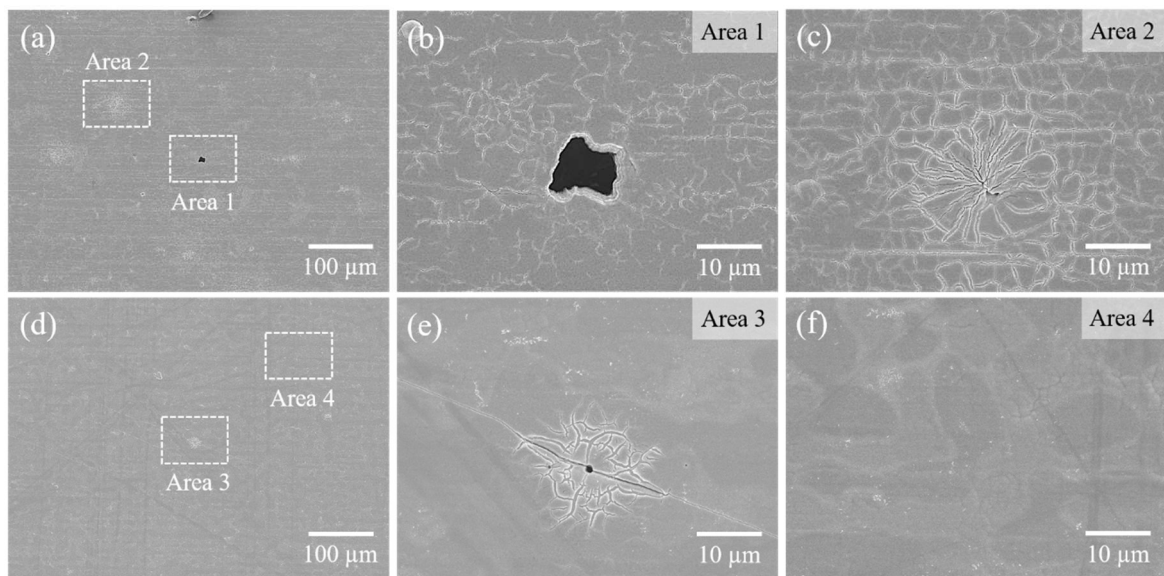


Fig. 13 Surface FE-SEM images after potentiodynamic polarization until +2.5 V: (a) low magnification image of binary Fe-W alloy, (b) enlarged image of area 1, (c) enlarged image of area 2, (d) low magnification image of ternary Fe-W-Zn alloy deposited at pH 8.0, (e) enlarged image of area 3 and (f) enlarged image of area 4.